The Journal of Chemical Physics

RESEARCH ARTICLE | MARCH 02 2026

# Quantifying electron correlation effects in ethanol decomposition pathways

L. Cândido ; G.-Q. Hai



*J. Chem. Phys.* 164, 094302 (2026)
https://doi.org/10.1063/5.0315750

The Journal of Chemical Physics ARTICLE pubs.aip.org/aip/jcp

# Quantifying electron correlation effects in ethanol decomposition pathways

Cite as: J. Chem. Phys. 164, 094302 (2026); doi: 10.1063/5.0315750
Submitted: 8 December 2025 • Accepted: 13 February 2026 •
Published Online: 2 March 2026



L. Cândido[1,2,a)] and G.-Q. Hai[2]

## AFFILIATIONS

[1] Instituto de Física, Universidade Federal de Goiás, 74001-970 Goiânia, GO, Brazil
[2] Instituto de Física de São Carlos, Universidade de São Paulo, 13560-970 São Carlos, SP, Brazil

[a)] **Author to whom correspondence should be addressed:** ladir@ufg.br

## ABSTRACT

Ethanol decomposition is a prototypical multichannel organic reaction in which electron correlation plays a decisive role in determining activation barriers and reaction selectivity. We use fixed-node diffusion Monte Carlo (FN-DMC) to investigate three principal decomposition pathways: dehydration, C–C bond cleavage, and $H_2$ elimination. The obtained results are compared with those from Hartree–Fock (HF), hybrid density functional theory (B3LYP), modified Gaussian-2 composite theory, and experimental kinetic data. By recovering the missing many-body correlation, FN-DMC lowers the HF forward activation barriers by 4–15 kcal $mol^{-1}$ and yields barrier heights that are consistent with available Arrhenius activation parameters within expected thermal corrections. A correlation-energy analysis along the intrinsic reaction coordinate reveals a pathway-dependent modulation of dynamical correlation near the transition state, with the largest stabilization observed for the dehydration channel. The results demonstrate that FN-DMC provides a robust description of static activation barriers and offers mechanistic insight into the evolution of electron-correlation effects in complex bond-breaking reactions.





## I. INTRODUCTION

Ethanol decomposition serves as a prototype system for studying the interplay of bond breaking, hydrogen transfer, and electron correlation in multichannel organic reactions. Its conversion into smaller molecules through dehydration to ethylene and water or through C–C bond-scission routes is of both industrial and fundamental interest.[1–5] Accurate characterization of these competing channels provides insight into reaction selectivity and energy-conversion efficiency, and has motivated extensive experimental investigations based on shock-tube, flow-reactor, and kinetic-model analyses,[3,6–11] as well as studies combining detailed experiments with *ab initio* calculations.[6] Early theoretical work and subsequent high-level modeling studies have further clarified the underlying reaction mechanisms and energetics.[12]

Electron correlation, arising from many-body interactions beyond the mean field, plays a decisive role in determining transition-state (TS) stability and overall reaction energetics. Hartree–Fock (HF) theory, which neglects correlation, provides a useful reference but tends to overestimate energy barriers and fails to capture subtle electronic effects critical along the reaction pathway.[13] The density functional theory (DFT), which includes correlation approximately via exchange–correlation functionals,[14–16] offers valuable orbital-level insights into the evolving electronic structure. However, the accuracy of DFT depends sensitively on the chosen exchange–correlation functional, and even for reactions with sizable activation barriers, independent benchmarks based on explicitly correlated many-body methods remain valuable for assessing transition-state energetics. In this context, composite approaches, such as modified Gaussian-2 (G2M),[17] which are based on CCSD(T) electronic energies, provide an important reference, while FN-DMC offers a complementary, parameter-free many-body framework for evaluating electron-correlation effects.

Quantum Monte Carlo (QMC) methods offer one of the most accurate treatments of electron correlation,[18–21] enabling a reliable description of reaction energetics and transition-state stabilization. Despite extensive experimental, kinetic, and DFT-based studies, a quantitatively reliable benchmark for transition-state stabilization due to explicit electron correlation in ethanol decomposition remains lacking. Fixed-node diffusion Monte Carlo (FN-DMC) provides a systematically improvable, many-body approach for addressing this challenge. FN-DMC has been successfully applied

to reaction energetics and barrier heights in a variety of molecular systems, yielding chemically accurate trends and, in favorable cases, near-chemical accuracy relative to experiment,[21–23] including bond-breaking processes and transition states, as demonstrated in earlier work by Guidoni and co-workers and by Filippi and collaborators.[24–28] In this framework, the accuracy of FN-DMC depends on the quality of the nodal surface of the trial wave function, while remaining free of empirical parameters in the treatment of electron correlation.

Here, we employ FN-DMC to quantify the role of electron correlation in the energetics of ethanol decomposition pathways and to provide a benchmark for commonly used electronic-structure methods. By comparing QMC results with those from HF, which neglects correlation, we can explicitly determine the stabilization provided by correlation for key energetic quantities: the activation barrier (from reactants to the TS), the reverse barrier (from products to the TS), and the overall reaction energy (from reactants to products). In this way, QMC quantifies how electron correlation lowers the TS energy relative to both reactants and products. Benchmarking DFT against QMC further refines our understanding of the potential energy surface and provides a rigorous foundation for assessing correlation effects on reaction energetics and pathways.

A quantitatively accurate description of correlation effects along reaction coordinates is essential for developing reliable theoretical models of gas-phase reaction energetics. The present analysis provides detailed insight into how dynamic and static correlation contributions evolve through bond breaking and bond formation in multichannel reaction pathways. Such understanding is fundamental for assessing the performance of electronic-structure methods and for establishing FN-DMC as a benchmark approach for transition-state energetics in chemically relevant systems.

## II. COMPUTATIONAL DETAILS

The ethanol decomposition pathways for reaction 1 ($C_2H_5OH \rightarrow C_2H_4 + H_2O$), reaction 2 ($C_2H_5OH \rightarrow CH_4 + CHOH$), and reaction 3 ($C_2H_5OH \rightarrow C_2H_4O + H_2$) are investigated using initial geometries obtained by optimizing the expected reactants and products from prior theoretical studies.[5] Geometries for reactants, products, and TSs are re-optimized at the B3LYP/cc-pVQZ level, and all TSs are confirmed by frequency analysis showing a single imaginary mode using the Gaussian16[29] package. The TS frequencies are −2009.97, −1062.70, and −1196.79 $cm^{-1}$ for reactions 1, 2, and 3, respectively. Intrinsic reaction coordinate (IRC) calculations verify the connection between minima and TSs.[30] IRC calculations were performed at the restricted B3LYP/cc-pVQZ level to define a smooth, spin-pure reference reaction path. Single-point HF and FN-DMC energies were subsequently evaluated at selected geometries along these IRCs. Although unrestricted HF (UHF) calculations were tested to allow for possible spin-symmetry breaking along bond-breaking coordinates, all such calculations converged to spin-pure singlet solutions for the geometries considered in this work. This indicates that spin-symmetry breaking is not observed along the reaction paths studied here and supports the use of restricted references in the transition-state region.

Therefore, the resulting B3LYP geometries were adopted as reference configurations for the QMC calculations. The choice of B3LYP/cc-pVQZ geometries reflects a balance between accuracy, computational feasibility, and consistency with both composite methods and established quantum Monte Carlo practice. B3LYP has been extensively validated for oxygenated hydrocarbons and is known to provide reliable equilibrium and transition-state geometries for reactions involving C–O bond cleavage, hydrogen transfer, and dehydration processes.[31] Moreover, B3LYP geometries are commonly employed as reference structures in composite approaches such as G2M and in FN-DMC studies, ensuring methodological consistency across the comparisons presented here.

All-electron QMC simulations are performed using the CASINO code.[32] Initially, variational Monte Carlo (VMC) is used to optimize a correlated many-body trial wavefunction, expressed as the product of Slater determinants for spin-up and spin-down orbitals multiplied by an explicit Jastrow correlation factor,

$$\Psi_T(R) = D_\uparrow(\{\phi_i\})\, D_\downarrow(\{\phi_i\}) e^J. \tag{1}$$

Here, $R$ denotes the electronic configuration, and $\phi_i$ are the single-electron orbitals extracted from the DFT/B3LYP calculations. The Jastrow factor $J$ entering Eq. (1), $J = \sum_{i<j} u(r_{ij}) + \sum_{I,i} \chi_I(r_{iI}) + \sum_{I,i<j} f_I(r_{iI}, r_{jI}, r_{ij})$, was constructed following the standard CASINO functional form as a sum of electron–electron ($u$), electron–nucleus ($\chi$), and electron–electron–nucleus ($f$) correlation terms,[33] where $i$ and $j$ are index electrons, $I$ are indexes atomic cores, and $r_{iI}$, $r_{jI}$, and $r_{ij}$ are the corresponding distances. Polynomial expansions up to fourth order were employed for the electron–electron and electron–nucleus contributions, while the electron–electron–nucleus term included second-order electron–electron and electron–nucleus polynomials. Depending on the system (reactant, transition state, or product), the total number of optimizable Jastrow parameters ranged from ~40 to 80. All Jastrow parameters were optimized by energy minimization using the linear optimization scheme as implemented in the CASINO code.[34,35] The Gaussian orbitals in the Slater determinants are adjusted to satisfy the electron–nucleus cusp condition.[36]

Subsequently, diffusion Monte Carlo (DMC) simulations are performed to eliminate the remaining variational bias. In these simulations, the optimized trial wavefunction serves as a guiding function for importance sampling, while the imaginary-time propagator, $e^{-\tau H}$, is iteratively applied (using a short-time approximation) to project the trial wavefunction onto the ground state. We employed the fixed-node (FN-DMC) approximation[37,38] to constrain the nodes of the DMC solution to those of the trial wavefunction.

A key advantage of FN-DMC over mean-field methods such as HF and DFT is its relatively weak dependence on the basis set, as it directly samples many-body wavefunctions in real space. Instead, the fixed-node approximation is the primary source of systematic error in FN-DMC calculations. Since we employ single-determinant trial wavefunctions obtained from DFT, the accuracy of FN-DMC energies depends on the chosen exchange-correlation functional. Hybrid functionals, such as B3LYP,[15,39] which is used in this work, often yield improved nodal surfaces compared to pure GGA functionals, leading to better FN-DMC total energies and barrier heights. However, the extent to which the choice of DFT orbitals used to construct the trial wave function affects FN-DMC relative energies, such as activation barriers, remains to be systematically explored.

**TABLE I.** Computed forward and reverse barriers ($\Delta E_f$, $\Delta E_r$), reaction energies ($\Delta E_{rxn}$) (without ZPE corrections), and experimental apparent activation energies ($E_a$) for the ethanol decomposition pathways. Uncertainties are reported in parentheses for FN-DMC and experimental values. Experimental $E_a$ values were derived from Arrhenius fits to shock-tube, flow-reactor, and kinetic-model data under near-atmospheric conditions. All energies are given in kcal mol$^{-1}$.

| Reaction | Method | $\Delta E_f$ | $\Delta E_r$ | $\Delta E_{rxn}$ | References/source |
|---|---|---|---|---|---|
| 1: $C_2H_5OH \rightarrow C_2H_4 + H_2O$ | HF | 88.3 | 76.2 | 12.1 | This work |
| | BLYP | 60.8 | 50.2 | 10.6 | This work |
| | PBE | 61.0 | 44.0 | 17.0 | This work |
| | PBE0 | 69.3 | 50.6 | 18.7 | This work |
| | B3LYP | 67.6 | 54.3 | 13.3 | This work |
| | FN-DMC | 74.7(6) | 57.4(6) | 17.3(9) | This work |
| | G2M (RCC2) | 66.6 | ⋯ | ⋯ | Park *et al.*[12] |
| | Experiment ($E_a$) | 54(2) | ⋯ | ⋯ | Sivaramakrishnan *et al.*[6] |
| 2: $C_2H_5OH \rightarrow CH_4 + CHOH$ | HF | 112.2 | 53.7 | 58.5 | This work |
| | BLYP | 97.2 | 36.0 | 61.2 | This work |
| | PBE | 96.3 | 27.0 | 69.3 | This work |
| | PBE0 | 101.5 | 30.0 | 71.5 | This work |
| | B3LYP | 101.6 | 36.8 | 64.8 | This work |
| | FN-DMC | 108.0(6) | 36.3(5) | 71.7(8) | This work |
| | G2M (RCC2) | 85.7 | ⋯ | ⋯ | Park *et al.*[12] |
| | Experiment ($E_a$) | 128.7(5) | ⋯ | ⋯ | Li *et al.*[7] |
| 3: $C_2H_5OH \rightarrow C_2H_4O + H_2$ | HF | 128.8 | 107.2 | 21.6 | This work |
| | BLYP | 92.2 | 75.8 | 16.4 | This work |
| | PBE | 92.3 | 70.2 | 22.1 | This work |
| | PBE0 | 104.3 | 78.4 | 25.9 | This work |
| | B3LYP | 101.9 | 81.2 | 20.7 | This work |
| | FN-DMC | 113.8(6) | 86.9(6) | 26.9(9) | This work |
| | G2M (RCC2) | 86.1 | ⋯ | ⋯ | Park *et al.*[12] |
| | Experiment ($E_a$) | 92(10) | ⋯ | ⋯ | Marinov[3] |

For the FN-DMC calculations, we employed a small time step of 0.0001 Ha with a walker population of $10^4$, yielding acceptance ratios exceeding 99.9%. To assess time-step and population-control biases, we performed convergence tests using larger time steps in the range of 0.001–0.0005 Ha for representative geometries and verified that the FN-DMC energies vary linearly with the time step in this regime. At sufficiently small time steps, the DMC time-step bias is approximately linear in the time step, while the finite-population bias scales inversely with the number of walkers.[40,41] Therefore, we linearly extrapolated selected test calculations to the zero-time-step limit, confirming that residual biases at 0.0001 Ha with $10^4$ walkers are well below the statistical uncertainty. Production runs comprised $2.5 \times 10^5$ to $2.0 \times 10^6$ DMC steps, yielding statistical uncertainties of $4 \times 10^{-4}$ to $8 \times 10^{-4}$ Ha in total energies, corresponding to uncertainties below 1 kcal mol$^{-1}$ in the activation and reaction energies reported in Table I (see the supplementary material). Barrier energies reported in Table I were converted to kcal mol$^{-1}$ using 1 Ha = 627.509 kcal mol$^{-1}$.

Finally, by comparing FN-DMC energies with HF/cc-pV6Z energies along the reference IRC, we directly quantify the contribution of electron correlation to TS stabilization and barrier reduction. This integrated computational strategy not only ensures the reliability of our simulation results but also provides a robust framework for exploring the influence of electron correlation on the kinetics and thermodynamics of ethanol decomposition.

## III. RESULTS AND DISCUSSIONS

The energy profiles for the three ethanol decomposition reactions were computed using HF, DFT/B3LYP, and FN-DMC. Figures 1–3 show the relative energies along the intrinsic reaction coordinate (IRC), reported here as an IRC path length. The horizontal axis represents progression along the intrinsic reaction coordinate; numerical values are omitted because the IRC integration formally connects only the TS to the adjacent minima (the reactant and product structures are not part of the IRC integration itself). The IRC represents the cumulative mass-weighted displacement along the steepest-descent path from the transition state in nuclear configuration space, as defined in Fukui's formalism[30] and implemented in Gaussian.[29] To provide a direct structural interpretation of this coordinate, the lower panels of Figs. 1–3 show the evolution of selected key bond lengths plotted as a function of the IRC path length (or IRC step index). These bond distances explicitly illustrate the bond-breaking and bond-forming processes that define each reaction pathway. In each figure, the TS is identified with the maximum along the IRC; the reactant lies to the left and the products to the right. To provide smooth asymptotic references, the dashed segments indicate where the curves depart from the IRC trace and are continued by standard geometry optimizations of the reactant and product states performed beyond the last converged IRC point.

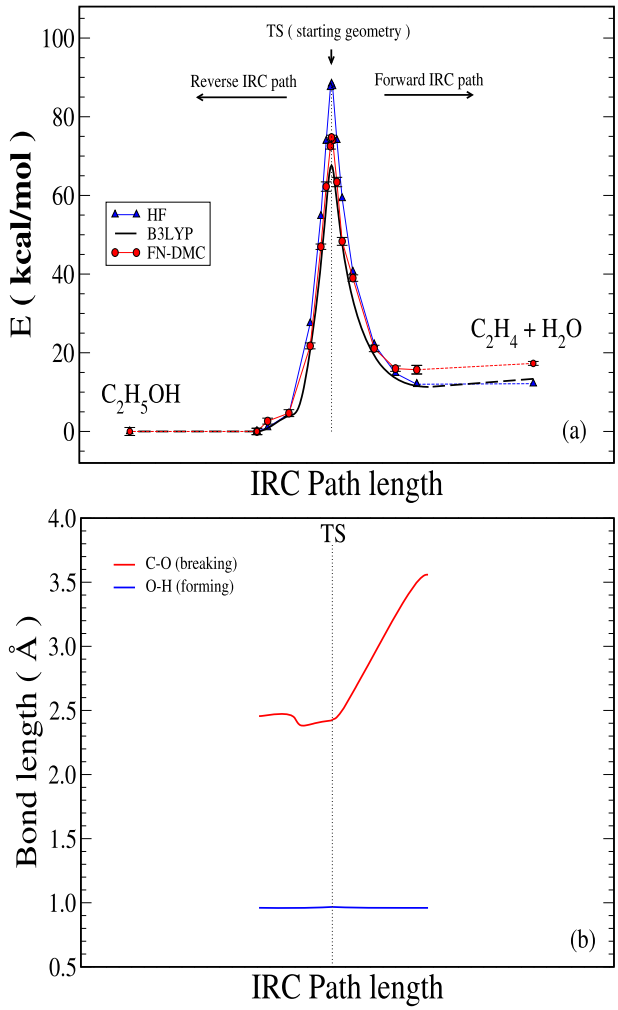


**FIG. 1.** (a) Relative energy (kcal mol$^{-1}$) along the IRC for ethanol dehydration, with the reactant taken as the zero of energy. Results from FN-DMC, HF, and DFT are shown. Molecular structures corresponding to the reactant, transition state, and product are indicated. (b) Evolution of key bond lengths (in Å) along the IRC, plotted as a function of the IRC path length: the breaking C–O bond and the forming O–H bond of water. The TS region is indicated by a vertical dashed line.

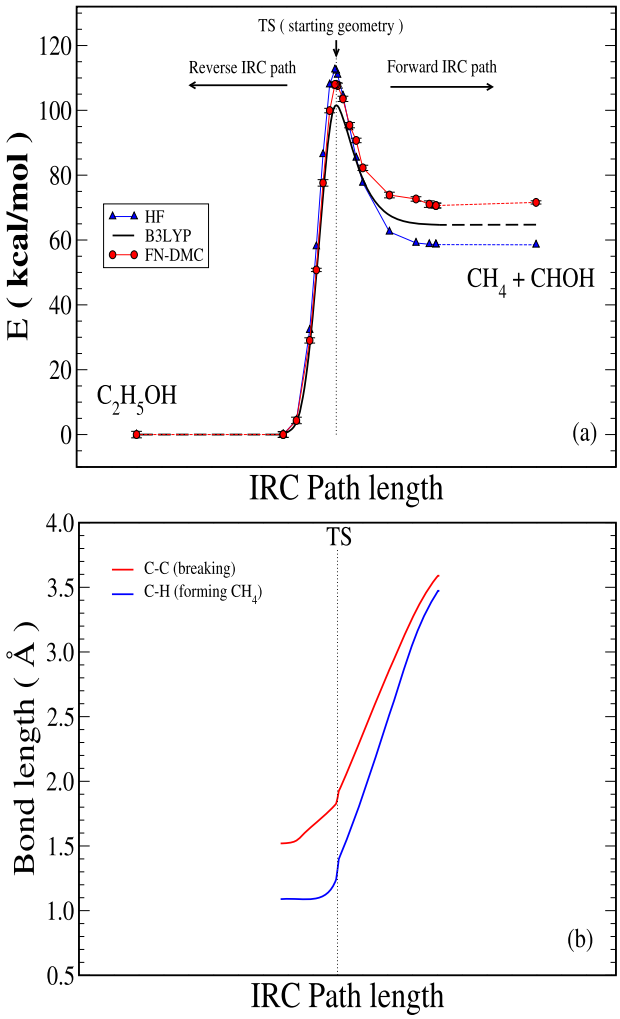


**FIG. 2.** (a) Relative energy (in kcal mol$^{-1}$) along the IRC for the C–C bond cleavage pathway of ethanol leading to methane and CHOH, with the reactant taken as the zero of energy. Results from FN-DMC, HF, and DFT are shown. Molecular structures corresponding to the reactant, transition state, and product are indicated. (b) Evolution of key bond lengths (in Å) along the IRC, plotted as a function of the IRC step index: the breaking C–C bond and the forming C–H bond associated with $CH_4$ formation. The TS region is indicated by a vertical dashed line.

With this convention, the forward and reverse barrier heights are defined as $\Delta E_f = E_{TS} - E_R$ and $\Delta E_r = E_{TS} - E_P$, respectively, and the reaction energy is given by the following relation:

$$\Delta E_{rxn} = E_P - E_R = \Delta E_f - \Delta E_r. \quad (2)$$

Hence, when $\Delta E_f > \Delta E_r$, the reaction is endothermic ($\Delta E_{rxn} > 0$), i.e., energy must be absorbed to convert reactants into products.

Figure 1(a) displays the energy profile for the dehydration of ethanol (reaction 1: $C_2H_5OH \rightarrow C_2H_4 + H_2O$). The transition state (TS) corresponds to the maximum along the IRC path, with HF predicting a forward barrier of 88.3 kcal mol$^{-1}$, DFT/B3LYP yielding 67.6 kcal mol$^{-1}$, and FN-DMC giving 74.7(6) kcal mol$^{-1}$. The product minimum lies above the reactant baseline, with a reaction energy of $\Delta E_{rxn} = +17.3(9)$ kcal mol$^{-1}$, confirming its endothermic nature. FN-DMC lowers the forward barrier by about 15.4% relative to HF, demonstrating the role of electron correlation in stabilizing the TS. Figure 1(b) illustrates the evolution of key bond lengths along the reaction coordinate, highlighting the breaking of the C–O bond and the concomitant formation of the O–H bond at the transition state.

Figure 2(a) shows a similar trend for the C–C bond-cleavage pathway (reaction 2: $C_2H_5OH \rightarrow CH_4 + CHOH$). HF predicts a forward barrier of 112.2 kcal mol$^{-1}$, while DFT and FN-DMC give

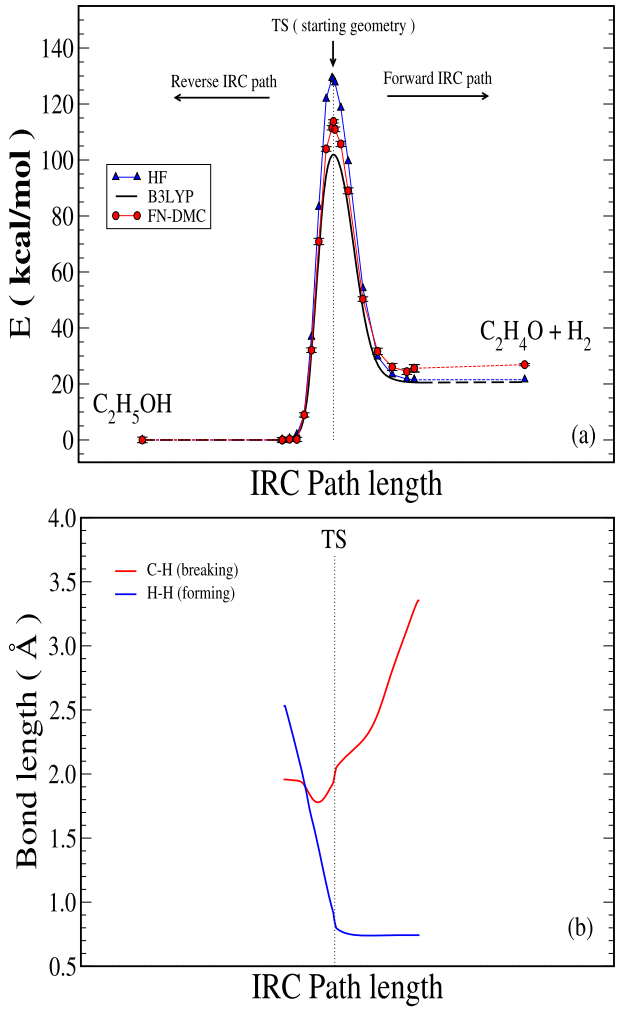


**FIG. 3.** (a) Relative energy (in kcal mol$^{-1}$) along the IRC for the $H_2$-elimination pathway, with the reactant taken as the zero of energy. Results from FN-DMC, HF, and DFT are shown. Molecular structures corresponding to the reactant, transition state, and product are indicated along the energy profile. (b) Evolution of key bond lengths (in Å) along the IRC path progression: the breaking C–H bond and the forming H–H bond associated with molecular hydrogen formation. The TS region is indicated by a vertical dashed line.

101.6 and 108.0(6) kcal mol$^{-1}$, respectively. The products lie significantly above the reactant baseline, yielding $\Delta E_{rxn}$ = +71.7(8) kcal mol$^{-1}$, again indicating an endothermic process. FN-DMC reduces the HF barrier by about 4 kcal mol$^{-1}$ (≈3.7%), highlighting notable dynamic correlation effects associated with simultaneous C–O and C–C bond reorganization. Figure 2(b) tracks the breaking C–C bond and the simultaneous formation of the C–H bond leading to $CH_4$, providing a clear structural interpretation of the transition state associated with this pathway.

As shown in Fig. 3(a), the $H_2$-elimination reaction is also endothermic. FN-DMC yields a forward barrier of 113.8(6) kcal mol$^{-1}$ and a reverse barrier of 86.9(6) kcal mol$^{-1}$, giving $\Delta E_{rxn}$ = 26.9(9) kcal mol$^{-1}$. Here, $\Delta E_f > \Delta E_r$, consistent with the positive reaction energy. Electron correlation stabilizes the transition state more than the reactant $\Delta E_{corr} \approx -15.0$ kcal mol$^{-1}$, yielding a moderate reduction of the forward barrier. Figure 3(b) shows the elongation of the C–H bond and the formation of the H–H bond, directly linking the computed energy barrier to the microscopic mechanism of $H_2$ formation.

Across all three pathways, the FN-DMC reaction barriers are systematically ≈4–15 kcal mol$^{-1}$ lower than those from HF calculations. These FN-DMC values are close to those obtained from composite G2M calculations and are consistent with experimental kinetic estimates, as shown in Table I. The consistent trend, $\Delta E_f > \Delta E_r$ for all channels, confirms that the ethanol decomposition reactions are endothermic under standard conditions. They require external energy to cleave strong C–O, C–C, and O–H bonds. Furthermore, electron correlation plays a key role in stabilizing the transition states that govern the reaction kinetics and mechanisms.

FN-DMC provides a parameter-free many-body reference for assessing DFT predictions of activation barriers. Differences between FN-DMC and DFT arise from both the approximate nodal structure of single-determinant trial wave functions in FN-DMC and the limitations of approximate exchange–correlation functionals within the Kohn–Sham framework. Comparison across multiple functionals (BLYP, PBE, PBE0, and B3LYP), as summarized in Table I and detailed further in the supplementary material (Tables S1–S3), reveals systematic functional-dependent deviations in barrier heights. Semi-local functionals tend to underestimate the forward barriers relative to FN-DMC, while hybrid functionals partially recover the missing stabilization but remain method-dependent, underscoring the complementary nature of FN-DMC and DFT approaches.

Table I summarizes the computed forward and reverse energy barriers, reaction energies, and the corresponding experimental apparent activation energies. The experimental $E_a$ values reported in the table were extracted from Arrhenius fits to shock-tube,[6] flow-reactor,[7] and kinetic-model[3] measurements under near-atmospheric conditions. As shown in Table I, the FN-DMC forward barriers are 4.2–15 kcal mol$^{-1}$ lower than the HF values, bringing the FN-DMC results into closer agreement with both G2M benchmark calculations and the experimental Arrhenius activation energies.

For the dehydration pathway ($C_2H_5OH \rightarrow C_2H_4 + H_2O$),[6] measured absolute rate constants using a reflected shock-tube setup, where ethanol–argon mixtures were heated for microseconds at 1200–1600 K. Time-resolved infrared absorption profiles of $H_2O$ and $C_2H_4$ were analyzed using detailed kinetic modeling and fitted to a single-step Arrhenius expression,

$$k(T) = A \exp(-E_a/RT), \quad (3)$$

yielding an apparent activation energy of $E_a$ = 54 ± 2 kcal mol$^{-1}$ near the high-pressure limit, where $A$ is the pre-exponential factor, $R$ is the universal gas constant (8.314 J mol$^{-1}$ K$^{-1}$), and $T$ is the absolute temperature. The FN-DMC forward barrier of 74.7(6) kcal mol$^{-1}$ is ~14 kcal mol$^{-1}$ lower than the HF result and agrees with the G2M value.[12] The smaller experimental activation energy reflects thermal and entropic effects absent from the 0 K potential energy surface. The correlation-driven TS stabilization captured by FN-DMC accounts for the residual difference between the computed static barrier and the kinetic estimate.

For the C–C bond-cleavage pathway ($C_2H_5OH \rightarrow CH_4 + CHOH$),[7] combined flow-reactor experiments (900–1100 K) with RRKM/master-equation modeling to fit measured species profiles. The extracted modified Arrhenius expression for the rate constant is

$$k(T) = 6.4 \times 10^{34}\ T^{-9.16}\ \exp(-64\,751/T)\ \mathrm{s}^{-1}, \quad (4)$$

which corresponds to $E_a = 128.7(5)$ kcal mol$^{-1}$. The FN-DMC barrier of 108.0(6) kcal mol$^{-1}$ lies between the experimental and G2M results, indicating that the QMC barrier represents the intrinsic 0 K threshold, while the experimental $E_a$ includes temperature and fall-off corrections. Electron correlation reduces the HF barrier by roughly 4 kcal mol$^{-1}$, confirming its crucial role in accurately describing C–C bond scission energetics.

For the endothermic $H_2$-elimination reaction ($C_2H_5OH \rightarrow C_2H_4O + H_2$), Ref. 3 inferred an activation energy of $E_a = 92(10)$ kcal mol$^{-1}$ by optimizing a kinetic model against ignition-delay and flame-speed data. The FN-DMC forward barrier is 113.8(6) kcal mol$^{-1}$, with a reverse barrier of 86.9(6) kcal mol$^{-1}$. These values are consistent with the reaction's endothermicity ($\Delta E_{\mathrm{reaction}} = 26.9(9)$ kcal mol$^{-1}$). The higher forward barrier compared to the experimental value likely reflects an incomplete treatment of static correlation in oxygenated transition states or the thermal averaging inherent in experimental rate fits.

Although experimental data are commonly reported as apparent activation energies ($E_a$) derived from high-temperature Arrhenius fits, these quantities differ from the 0 K potential-energy barriers computed here. For the dehydration and $H_2$-elimination channels (reactions 1 and 3), the experimental $E_a$ values are smaller because thermal and entropic effects lower the effective barrier height. To compare with the static potential-energy barriers, one must add the missing thermal corrections (typically 15–25 kcal mol$^{-1}$). In contrast, for the C–C bond-cleavage pathway (reaction 2), the measured $E_a$ already includes high-temperature energy contributions that elevate the apparent barrier, so the intrinsic 0 K potential barrier is smaller by a comparable amount. Hence, the direction of the correction depends on whether vibrational and entropic terms act to reduce (reactions 1 and 3) or increase (reaction 2) the observed kinetic barrier.

Overall, FN-DMC reproduces experimental trends and yields activation barriers that are consistent with available experimental and benchmark estimates for all reaction channels. The explicit treatment of electron correlation is essential for capturing TS stabilization and the balance between dynamic and static correlation. This capability allows FN-DMC to effectively bridge the gap between 0 K potential-energy profiles and finite-temperature experimental kinetics in ethanol thermal decomposition.

The electron-correlation energy is defined here as the energy gain obtained by including explicit many-body effects beyond the mean-field HF description,

$$E_{\mathrm{corr}} = E_{\mathrm{DMC}} - E_{\mathrm{HF}}, \quad (5)$$

where $E_{\mathrm{DMC}}$ is the FN-DMC energy, and $E_{\mathrm{HF}}$ is the corresponding HF energy evaluated at the same nuclear geometry. Because the FN-DMC calculations employ single-determinant trial wave functions constructed from B3LYP orbitals, this quantity should be interpreted as an effective correlation energy recovered beyond HF within the fixed-node approximation, rather than as the exact fixed-node correlation energy in a formal sense.

To analyze how correlation effects evolve along the reaction path, we define the position-dependent correlation contribution relative to the reactant as follows:

$$\Delta E_{\mathrm{corr}}(x) = (E_{\mathrm{DMC}} - E_{\mathrm{HF}})(x) - (E_{\mathrm{DMC}} - E_{\mathrm{HF}})_{\mathrm{R}}, \quad (6)$$

where $x$ denotes the intrinsic reaction coordinate and the subscript $R$ refers to the reactant geometry. This definition isolates the change in correlation stabilization along the reaction coordinate and enables a direct comparison of correlation effects at different stationary points.

Before addressing the detailed evolution of the correlation contribution along the reaction path in Fig. 4, it is important to recall that all total energies (HF, DFT, and FN-DMC) for the systems considered are negative. In the energy profiles of Figs. 1–3, each curve is shifted so that the reactant energy is set to zero, meaning that the plotted points represent differences relative to the reactant rather than absolute total energies. The same shift is implicitly inherited in the correlation–energy curve, for which $\Delta E_{\mathrm{corr}}(x) = E_{\mathrm{corr}}(x) - E_{\mathrm{corr}}(\mathrm{R})$. Under this convention, the sign of $\Delta E_{\mathrm{corr}}$ directly tracks how electron correlation changes along the IRC. Negative values near the transition state (TS) indicate that correlation stabilizes the TS more strongly than the reactant. In contrast, positive values observed beyond the TS reflect a reduced correlation gain in the product region, not an increase in total energy. The profile of $\Delta E_{\mathrm{corr}}$ from zero at the reactant to negative at the TS and then to positive values toward the products is consistent with the expected modulation of correlation strength as bonds stretch and re-form along the reaction coordinate.

Because the HF and FN-DMC energy profiles in Figs. 1–3 are each shifted so that their respective reactant energies are zero,

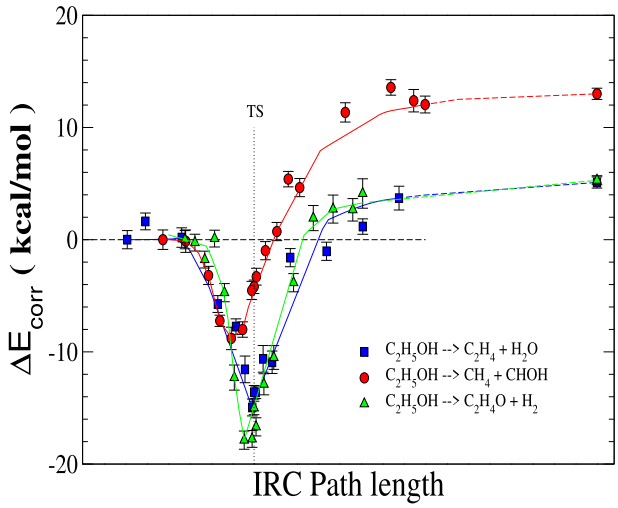


**FIG. 4.** Electron-correlation energy difference $\Delta E_{\mathrm{corr}}(x)$, along the intrinsic reaction coordinate for the three ethanol-decomposition pathways. Negative values indicate enhanced stabilization relative to HF. Dashed lines denote the transition from the IRC trace to fully optimized geometries. The TS location is indicated by the vertical dotted line.

the correlation-energy difference in Eq. (6) simplifies in the plotted representation. In this shifted frame, $\Delta E_{\mathrm{corr}}(x) = E_{\mathrm{corr}}(x)$, and therefore, $\Delta E_{\mathrm{corr}}(\mathrm{TS}) = E_{\mathrm{corr}}(\mathrm{TS})$. In an unshifted total-energy scale, the reactant correlation energy would enter explicitly, and the TS stabilization would be given by $\Delta E_{\mathrm{corr}}(\mathrm{TS}) = E_{\mathrm{corr}}(\mathrm{TS}) - E_{\mathrm{corr}}(\mathrm{R})$. The shifted representation is used here solely for clarity of visual comparison along the IRC and does not affect the numerical values of the TS correlation stabilization reported from the barrier heights (Table I).

A negative $\Delta E_{\mathrm{corr}}(x)$ indicates enhanced stabilization from electron correlation at a given point along the reaction path relative to the reactant state. Figure 4 illustrates how this stabilization evolves continuously along the IRC, reflecting the reorganization of electronic structure as chemical bonds stretch until they are broken. The location where the correlation curve intersects the vertical dotted line marks the transition state; although this figure is not used to determine the numerical TS stabilization, the values extracted from Table I are consistent with the behavior observed in Fig. 4. Using $\Delta E_{\mathrm{corr}}(\mathrm{TS}) = \Delta E_{\mathrm{f}}^{\mathrm{DMC}} - \Delta E_{\mathrm{f}}^{\mathrm{HF}}$, we find the values of $\Delta E_{\mathrm{corr}}(\mathrm{TS})$ are $-13.6$ kcal mol$^{-1}$ for reaction 1, $-4.2$ kcal mol$^{-1}$ for reaction 2, and $-15.0$ kcal mol$^{-1}$ for reaction 3. These results confirm that electron correlation is redistributed differently along the three IRCs, with the strongest TS stabilization in the dehydration and $H_2$-elimination channels (reactions 1 and 3), and a modest effect in the C–C bond-cleavage pathway (reaction 2).

We note that the minimum in $\Delta E_{\mathrm{corr}}(x)$ does not generally coincide with the maximum of the IRC path. This behavior reflects the fact that electron correlation responds primarily to changes in the electronic structure rather than to the barrier height itself. Along the IRC, the buildup of correlation is maximal when bonds are partially broken, and electrons become more delocalized or near-degenerate, which may occur slightly before or after the transition state depending on the reaction mechanism. Thus, while the TS indicates the kinetic bottleneck, the extrema in the correlation-energy profile reveal where electron reorganization plays the dominant stabilizing role along each decomposition pathway.

While reaction 2 exhibits the smallest correlation-induced reduction in the activation barrier, reaction 3 is of particular interest because it represents a qualitatively different regime of electron correlation. The differential correlation energy in reaction 3 ($C_2H_5OH \rightarrow C_2H_4O + H_2$) is moderate ($\Delta E_{\mathrm{corr}} \approx -15.0$ kcal mol$^{-1}$), yet its mechanistic origin differs from that of reactions 1 and 2. Two factors explain this behavior: (i) the pronounced endothermicity ($\Delta E_{\mathrm{reaction}} \approx +26.9$ kcal mol$^{-1}$), which keeps the products and TS relatively high on the potential-energy surface, and (ii) the partially multireference character of the oxygenated transition state, which limits the additional stabilization that single-determinant nodes can capture. Thus, although the correlation correction is larger than in reaction 2, it fails to compensate for the intrinsic thermodynamic penalty of this endothermic pathway.

The TS in reaction 3 exhibits a formaldehyde-like oxygenated motif in which near-degenerate electronic configurations (e.g., oxygen lone pairs interacting with adjacent bonds) introduce static correlation effects that are not fully described by single-determinant approaches (HF, DFT/B3LYP, or FN-DMC with a single determinant). Consistent with this, B3LYP underestimates the forward barrier relative to FN-DMC (Table I), as hybrid functionals tend to overemphasize dynamic correlation while neglecting static contributions. While FN-DMC recovers most of the dynamic correlation responsible for the observed $\Delta E_{\mathrm{corr}} \approx -15.0$ kcal mol$^{-1}$ reduction, further improvement would require multi-determinant QMC to capture the residual static correlation present in oxygenated, endothermic intermediates.[42–45]

This distinction highlights the complementary nature of dynamic correlation captured by FN-DMC and static correlation that may require multi-determinant expansions. Our results for the three decomposition channels confirm that explicit electron correlation plays a decisive role in lowering the TS barriers relative to HF and semi-local DFT predictions. The correlation stabilization obtained from FN-DMC follows the same systematic trend reported by Krongchon *et al.*[21] in their comprehensive benchmark of 19 non-hydrogen-transfer reactions, where FN-DMC reduced the mean absolute barrier error to within 1–2 kcal mol$^{-1}$. In both studies, the HF reference systematically overestimates and semi-local DFT functionals slightly underestimate activation energies, while FN-DMC recovers the missing dynamical correlation that governs TS stabilization. However, unlike the atom-transfer and substitution reactions examined by Krongchon *et al.*,[21] the present system involves coupled hydrogen-transfer and C–C bond-cleavage steps in a polyatomic molecule. This allows us to probe how correlation effects redistribute along the reaction coordinate in a chemically realistic environment.

The consistency between the FN-DMC activation barriers and the available experimental Arrhenius parameters indicates that an explicit treatment of electron correlation is essential for obtaining quantitatively reliable static barrier heights. Our findings extend the conclusions of Krongchon *et al.*[21] from small benchmark reactions to a multichannel organic decomposition pathway relevant to renewable-fuel chemistry, highlighting the predictive power of QMC for complex reaction networks.

## IV. CONCLUSIONS

FN-DMC provides a consistent and systematically correlated many-body description of electron-correlation effects in ethanol decomposition and consistently lowers the HF activation barriers, bringing them into closer agreement with both G2M benchmarks and experimental Arrhenius estimates. The differential correlation-energy analysis shows that dynamical correlation stabilizes the transition states to varying degrees across the three pathways, with the largest effect observed for the dehydration channel. For the oxygenated $H_2$-elimination transition state, the presence of residual static correlation suggests that multideterminant trial wave functions may further improve the nodal surface. These results highlight the importance of explicit many-body correlation in bond-breaking reactions and demonstrate the capability of QMC methods to provide high-level reference activation energies for complex, multichannel reaction mechanisms. Future work incorporating multideterminant nodes and finite-temperature free-energy corrections will enable more direct connections to experimental kinetic observables.

## SUPPLEMENTARY MATERIAL

The supplementary material provides additional computational details and extended data supporting the results discussed in the

main text. It includes total electronic energies for reactants, transition states, and products obtained from HF, DFT, and FN-DMC calculations (Table S1). All forward and reverse activation barriers and reaction energies reported in the main text are derived directly from these total electronic energies. The supplementary material also reports correlation energies at reactant, transition-state, and product geometries (Table S2), as well as correlation contributions to activation barriers and reaction energies (Table S3). Methodological clarifications, including basis-set choices, error propagation procedures, and definitions of correlation-energy measures, are provided to ensure transparency and reproducibility of the analysis.

## ACKNOWLEDGMENTS

This work was supported by the Conselho Nacional de Desenvolvimento Científico e Tecnológico (CNPq), the Fundação de Amparo à Pesquisa do Estado de Goiás (FAPEG), and the Fundação de Amparo à Pesquisa do Estado de São Paulo (FAPESP) under Grant No. 2024/13179-3. The authors thank LaMCAD/UFG for the computational resources and the National Laboratory for Scientific Computing (LNCC/MCTI, Brazil) for providing HPC resources of the SDumont supercomputer.

## AUTHOR DECLARATIONS

### Conflict of Interest

The authors have no conflicts to disclose.

### Author Contributions

**L. Cândido**: Conceptualization (equal); Data curation (equal); Formal analysis (equal); Funding acquisition (equal); Investigation (equal); Methodology (equal); Project administration (equal); Resources (equal); Software (equal); Supervision (equal); Validation (equal); Visualization (equal); Writing – original draft (equal); Writing – review & editing (equal). **G.-Q. Hai**: Conceptualization (equal); Data curation (equal); Formal analysis (equal); Funding acquisition (equal); Investigation (equal); Methodology (equal); Project administration (equal); Resources (equal); Software (equal); Supervision (equal); Validation (equal); Visualization (equal); Writing – original draft (equal); Writing – review & editing (equal).

## DATA AVAILABILITY

The data that support the findings of this study are available from the corresponding author upon reasonable request.

## REFERENCES

[1] M. Zhang and Y. Yu, Ind. Eng. Chem. Res. **52**, 9505 (2013).
[2] Y. Gao, L. Neal, D. Ding, W. Wu, C. Baroi, A. M. Gaffney, and F. Li, ACS Catal. **9**, 8592 (2019).
[3] N. M. Marinov, Int. J. Chem. Kinet. **31**, 183 (1999).
[4] Z. Zhao, J. Li, A. Kazakov, and F. L. Dryer, Int. J. Chem. Kinet. **37**, 282 (2005).
[5] L. V. Mattos, G. Jacobs, B. H. Davis, and F. B. Noronha, Chem. Rev. **112**, 4094 (2012).
[6] R. Sivaramakrishnan, M.-C. Su, J. V. Michael, S. J. Klippenstein, L. B. Harding, and B. Ruscic, J. Phys. Chem. A **114**, 9425 (2010).
[7] J. Li, A. Kazakov, and F. L. Dryer, Int. J. Chem. Kinet. **33**, 859 (2001).
[8] L. T. Pinzón, O. Mathieu, C. R. Mulvihill, I. Schoegl, and E. L. Petersen, Proc. Combust. Inst. **37**, 239 (2019).
[9] O. Mathieu, L. T. Pinzón, T. M. Atherley, C. R. Mulvihill, I. Schoel, and E. L. Petersen, Combust. Flame **208**, 313 (2019).
[10] J. Bugler, B. Marks, O. Mathieu, R. Archuleta, A. Camou, C. Grégoire, K. A. Heufer, E. L. Petersen, and H. J. Curran, Combust. Flame **163**, 138 (2016).
[11] E. Ranzi, A. Frassoldati, R. Grana, A. Cuoci, T. Faravelli, A. P. Kelley, and C. K. Law, Prog. Energy Combust. Sci. **38**, 468 (2012).
[12] J. Park, R. S. Zhu, and M.-C. Lin, J. Chem. Phys. **117**, 3224 (2002).
[13] T. Helgaker, P. Jorgensen, and J. Olsen, *Molecular Electronic-Structure Theory* (John Wiley & Sons, 2013).
[14] W. Kohn and L. J. Sham, Phys. Rev. **140**, A1133 (1965).
[15] A. D. Becke, J. Chem. Phys. **98**, 5648 (1993).
[16] J. P. Perdew, K. Burke, and M. Ernzerhof, Phys. Rev. Lett. **77**, 3865 (1996).
[17] A. M. Mebel, K. Morokuma, and M.-C. Lin, J. Chem. Phys. **103**, 7414 (1995).
[18] W. M. C. Foulkes, L. Mitas, R. J. Needs, and G. Rajagopal, Rev. Mod. Phys. **73**, 33 (2001).
[19] M. Dubecky, L. Mitas, and P. Jurecka, Chem. Rev. **116**, 5188 (2016).
[20] M. Dubecky, P. Jurecka, R. Derian, P. Hobza, M. Otyepka, and L. Mitas, J. Chem. Theory Comput. **9**, 4287 (2013).
[21] K. Krongchon, B. Busemeyer, and L. K. Wagner, J. Chem. Phys. **146**, 124129 (2017).
[22] J. B. Anderson, J. Chem. Phys. **144**, 166101 (2016).
[23] F. Fracchia, C. Filippi, and C. Amovilli, J. Chem. Theory Comput. **9**, 3453 (2013).
[24] M. Barborini and L. Guidoni, J. Chem. Phys. **137**, 224309 (2012).
[25] C. Filippi and C. J. Umrigar, J. Chem. Phys. **105**, 213 (1996).
[26] C. Filippi and C. J. Umrigar, Phys. Rev. B **61**, R16291 (2000).
[27] S. Saccani, C. Filippi, and S. Moroni, J. Chem. Phys. **138**, 084109 (2013).
[28] C. Filippi, S. B. Healy, P. Kratzer, E. Pehlke, and M. Scheffler, Phys. Rev. Lett. **89**, 166102 (2002).
[29] M. J. Frisch, G. W. Trucks, H. B. Schlegel, G. E. Scuseria, M. A. Robb, J. R. Cheeseman, G. Scalmani, V. Barone, B. Mennucci, G. A. Petersson, H. Nakatsuji, M. Caricato, X. Li, H. P. Hratchian, A. F. Izmaylov, J. Bloino, G. Zheng, J. L. Sonnenberg, M. Hada, M. Ehara, K. Toyota, R. Fukuda, J. Hasegawa, M. Ishida, T. Nakajima, Y. Honda, O. Kitao, H. Nakai, T. Vreven, J. A. Montgomery, Jr., J. E. Peralta, F. Ogliaro, M. Bearpark, J. J. Heyd, E. Brothers, K. N. Kudin, V. N. Staroverov, R. Kobayashi, J. Normand, K. Raghavachari, A. Rendell, J. C. Burant, S. S. Iyengar, J. Tomasi, M. Cossi, N. Rega, J. M. Millam, M. Klene, J. E. Knox, J. B. Cross, V. Bakken, C. Adamo, J. Jaramillo, R. Gomperts, R. E. Stratmann, O. Yazyev, A. J. Austin, R. Cammi, C. Pomelli, J. W. Ochterski, R. L. Martin, K. Morokuma, V. G. Zakrzewski, G. A. Voth, P. Salvador, J. J. Dannenberg, S. Dapprich, A. D. Daniels, V. Farkas, J. B. Foresman, J. V. Ortiz, J. Cioslowski, and D. J. Fox, *Gaussian 16, Revision B.01*, Gaussian, Inc., Wallingford CT, 2016.
[30] K. Fukui, J. Phys. Chem. **74**, 4161 (1970).
[31] P. J. Stephens, F. J. Devlin, C. F. Chabalowski, and M. J. Frisch, J. Phys. Chem. **98**, 11623 (1994).
[32] R. J. Needs, M. D. Towler, N. D. Drummond, P. López Ríos, and J. R. Trail, J. Chem. Phys. **152**, 154106 (2020).
[33] N. D. Drummond, M. D. Towler, and R. J. Needs, Phys. Rev. B **70**, 235119 (2004).
[34] C. J. Umrigar, J. Toulouse, C. Filippi, S. Sorella, and R. G. Hennig, Phys. Rev. Lett. **98**, 110201 (2007).
[35] N. D. Drummond and R. J. Needs, Phys. Rev. B **72**, 085124 (2005).
[36] A. Ma, M. D. Towler, N. D. Drummond, and R. J. Needs, J. Chem. Phys. **122**, 224322 (2005).
[37] J. B. Anderson, J. Chem. Phys. **65**, 4121 (1976).
[38] P. J. Reynolds, D. M. Ceperley, B. J. Alder, and W. A. Lester, Jr, J. Chem. Phys. **77**, 5593 (1982).

[39]C. Lee, W. Yang, and R. G. Parr, Phys. Rev. B **37**, 785 (1988).
[40]C. J. Umrigar, M. P. Nightingale, and K. J. Runge, J. Chem. Phys. **99**, 2865 (1993).
[41]N. D. Drummond, J. R. Trail, and R. J. Needs, Phys. Rev. B **94**, 165170 (2016).
[42]Y. Zhao and D. G. Truhlar, Theor. Chem. Acc. **120**, 215 (2008).
[43]X. Li and J. Paldus, J. Chem. Phys. **126**, 234303 (2007).
[44]K. H. Marti and M. Reiher, Phys. Chem. Chem. Phys. **13**, 6750 (2011).
[45]A. J. Cohen, P. Mori-Sánchez, and W. Yang, Chem. Rev. **112**, 289 (2012).